$Ce_{3-x}Mg_xCo_9$: Transformation of a Pauli Paramagnet into a Strong Permanent Magnet

Tej N. Lamichhane,[1,2,*] Valentin Taufour,[1,3] Andriy Palasyuk,[1] Qisheng Lin,[1]
Sergey L. Bud'ko,[1,2] and Paul C. Canfield[1,2]

[1]*Ames Laboratory, U.S. DOE, Ames, Iowa 50011, USA*
[2]*Department of Physics and Astronomy, Iowa State University, Ames, Iowa 50011, USA*
[3]*Department of Physics, University of California Davis, Davis, California 95616, USA*

(Received 31 October 2017; revised manuscript received 16 January 2018; published 23 February 2018)

We report on the synthesis of single-crystal and polycrystalline samples of $Ce_{3-x}Mg_xCo_9$ solid solution ($0 \leq x \lesssim 1.4$) and characterization of their structural and magnetic properties. The crystal structure remains rhombohedral in the whole composition range and Mg partially replaces Ce in the 6*c* site of the $CeCo_3$ structure. Ferromagnetism is induced by Mg substitutions starting as low as $x = 0.18$ and reaching a Curie temperature as high as 450 K for $x = 1.35$. Measurements on single crystals with $x = 1.34$ and $T_C = 440$ K indicate an axial magnetic anisotropy with an anisotropy field of 6 T and a magnetization of 6 μ_B/f.u. at 300 K. Coercicity is observed in the polycrystalline samples consistent with the observed axial magnetic anisotropy. Our discovery of ferromagnetism with large axial magnetic anisotropy induced by substituting a rare-earth element by Mg is a very promising result in the search of inexpensive permanent-magnet materials and suggests that other nonmagnetic phases, similar to $CeCo_3$, may also conceal nearby ferromagnetic phases.

DOI: 10.1103/PhysRevApplied.9.024023

I. INTRODUCTION

Current rare-earth-based commercial magnets contain local-moment-bearing rare-earth elements, mainly Nd, Sm, and Dy, whose availability is, according to the U.S. Department of Energy, important to the clean-energy economy, and these magnets have an associated supply risk. Alternative to finding a long-sought rare-earth free, high-flux permanent magnet, attempts to find Ce-based permanent magnets or substituting Ce for more critical rare-earth elements could be a pragmatic strategy to address the criticality problem since Ce is a relatively more abundant rare-earth element [1] with an easier extraction chemistry. Ce is relatively easy to separate from the other rare-earth elements since it can easily be oxidized to CeO_2 via roasting from which it can be precipitated out in acidic solutions [2,3]. Ce can be, in theory as well as experiment, a substitute for critical rare-earth elements without much compromise in magnetic properties [4]. Because of the volatile price of critical rare-earth elements, Ce has drawn attention for developing gap magnets which will populate the gap in energy product (in the range of 10–20 MGOe) between low-flux (alnico, ferrites) and commercial rare-earth-based magnets such as $SmCo_5$ and $Nd_2Fe_{14}B$. Additionally, the study of new Ce-based compounds often can reveal interesting physics; Ce exhibits diverse electronic and magnetic properties like local-moment-bearing Ce^{3+} ions, nonmagnetic Ce^{4+} ions, mixed valency, intermediate valence state, and itinerant magnetism.

$Ce_{3-x}Mg_xCo_9$ alloys are substitute derivatives of $CeCo_3$ in which Mg partially replaces Ce in the 6*c* position. The hydrogenation properties of the compound Ce_2MgCo_9 ($x = 1$) and $Nd_{3-x}Mg_xCo_9$ alloys ($x \leq 1.5$) have recently been investigated [5,6]. In addition, it was shown that the substitution of Mg for Nd increases the Curie temperature from 381 K for $NdCo_3$ [7] to 633 K for Nd_2MgCo_9 [6].

In this work, we present the structural and magnetic properties of both single-crystal and polycrystalline $Ce_{3-x}Mg_xCo_9$ for $0 \leq x \lesssim 1.4$. The anisotropic magnetic properties are studied for a single crystal of $Ce_{1.662(4)}Mg_{1.338(4)}Co_9$. (Hereafter, we round off the single-crystal composition to three significant digits as $Ce_{1.66}Mg_{1.34}Co_9$.) We find a remarkable transformation of Pauli paramagnet $CeCo_3$ (Ce_3Co_9) into the potential permanent magnet $Ce_{3-x}Mg_xCo_9$, which develops 2.2 MJ/m^3 of uniaxial anisotropy energy at 2 K for $Ce_{1.66}Mg_{1.34}Co_9$.

II. EXPERIMENTAL METHODS

To establish the existence range of the solid solution $Ce_{3-x}Mg_xCo_9$, we prepare polycrystals with various nominal compositions of $0 \leq x \leq 2.00$ (see Table III). Ce metal from the Ames Laboratory Material Preparation Center (purity > 99.99%), Co chunks (99.95%, Alfa Aesar), and Mg (99.95%, Gallium Source) are packed in a three-capped Ta crucible [8] under an Ar atmosphere. The Ta crucible is then sealed into an amorphous silica ampoule. The ampoule

*tejl@iastate.edu

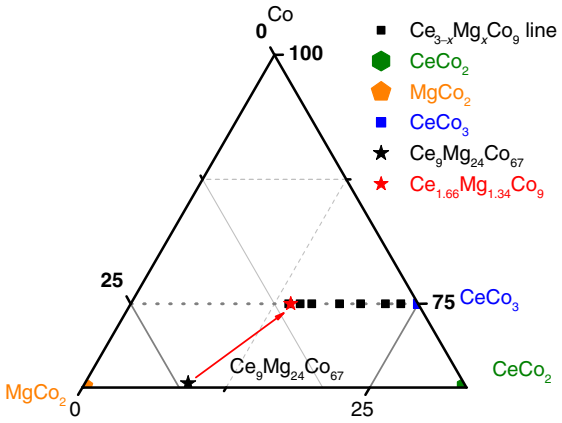

FIG. 1. Co-rich portion of the Co-Mg-Ce ternary phase diagram showing the $Ce_{3-x}Mg_xCo_9$ solid solution line and (1:2)-type impurity phases. $Ce_9Mg_{24}Co_{67}$ is the optimized initial melt composition for the solution growth of single-crystal $Ce_{1.66}Mg_{1.34}Co_9$. (See the text for details.)

is heated to 900 °C over 3 h and held there for 3 h. This step allows the reaction of Ce and Mg at low temperature and avoids the excessive boiling of Mg inside the Ta crucible. The ampoule is then heated to 1200 °C over 3 h and held there for 10 h. At this point, the ampoule is spun in a centrifuge, and all of the molten growth material is decanted and quenched in the catch side of the Ta tube. This step confirms that the mixture is forming a homogeneous melt at 1200 °C. The ampoule is put back into a furnace, then annealed at 900 °C for 24 h. Mg-free $CeCo_3$ is also synthesized by arc melting the stoichiometric composition and annealing at 900 °C for 1 week.

Single crystals of $Ce_{3-x}Mg_xCo_9$ are grown using a solution growth technique. An initial composition of $Ce_9Mg_{24}Co_{67}$ (see Fig. 1) is packed in a three-capped Ta crucible [8] and heated to 1200 °C similar to the polycrystals. The ampoule is then cooled down to 1100 °C over 75 h after which crystals are separated from the flux by using a centrifuge. Similarly, $CeCo_3$ single crystals are prepared by cooling a $Ce_{30}Co_{70}$ melt from 1200 °C to 1100 °C in 1 h and then to 1050 °C over 75 h [9].

Elemental analysis of the samples is performed using energy-dispersive spectroscopy (EDS). Polycrystalline samples are embedded in epoxy resin and finely polished. The polished samples are examined with EDS on six to ten spots and a statistical average composition is reported. Thin, platelike single-crystal samples [see Fig. 2(a)] are mounted on a conducting carbon tape. Self-flux-grown $MgCo_2$ and $CeCo_2$ single crystals are used as absorption standards for the Ce-Co-Mg alloy composition analyses. Powder x-ray-diffraction data are collected at room temperature on a Rigaku MiniFlex II diffractometer with Cu-$K\alpha$ radiation. Data are collected with a 3-s dwell time for each interval of 0.01° within a 2θ range of 10°–100°. Lattice parameters are refined by the Rietveld analysis method using the General Structure Analysis System [10] and EXPGUI [11].

Single-crystal x-ray diffraction is carried out on a Bruker Smart APEX II diffractometer with graphite-monochromatized Mo-$K\alpha$ radiation (0.710 73 Å). Reflections are gathered at room temperature by taking four sets of 360 frames with 0.5° scans in ω, with an exposure time of 10 s. The crystal-to-detector distance is

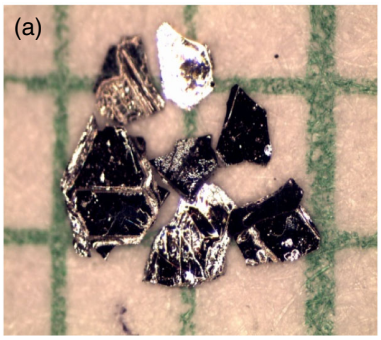

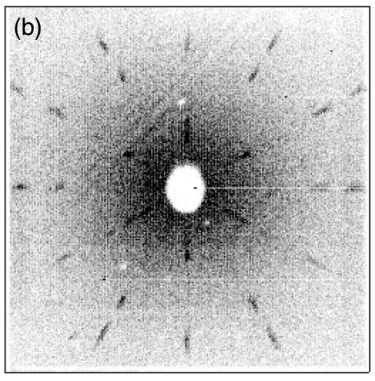

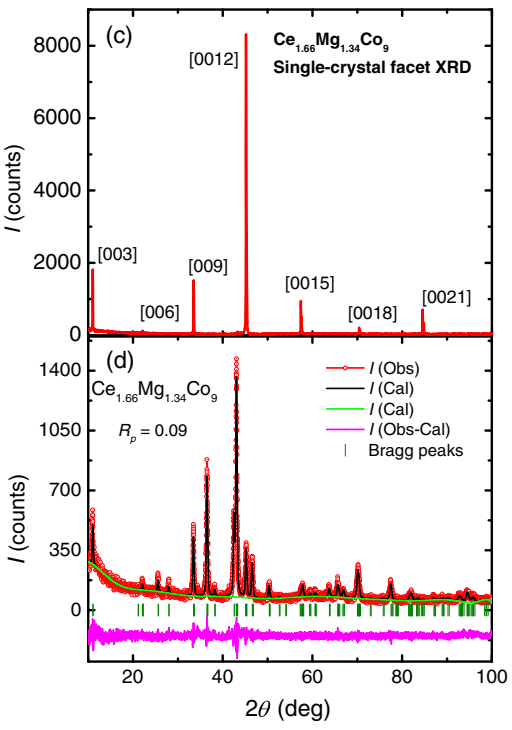

FIG. 2. (a) Single crystals of $Ce_{1.66}Mg_{1.34}Co_9$. (b) Backscattered Laue photograph of $Ce_{1.66}Mg_{1.34}Co_9$ with an x-ray beam perpendicular to the plate. (c) Monochromatic x-ray diffraction from the surface of a single crystal using Bragg-Brentano geometry. (d) Powder XRD for $Ce_{1.66}Mg_{1.34}Co_9$ where I (Obs), I (Cal), and I (Bkg) are the experimental, Rietveld refined, and instrumental background data, respectively. The lower section of the graph shows the Bragg's-peak positions with olive vertical lines and the differential x-ray diffractrogram I (Obs-Cal).

TABLE I. Crystallographic data and refinement parameters for $Ce_{1.662(4)}Mg_{1.338(4)}Co_9$.

Empirical formula	$Ce_{1.662(4)}Mg_{1.338(4)}Co_9$
Formula weight	796.32
Crystal system, space group	Trigonal, R-3m h
Unit-cell dimensions	$a = 4.9260(7)$ Å $c = 24.019(5)$ Å
Volume	504.75(18) Å^3
Z, calculated density	3, 7.859 g/cm^3
Absorption coefficient	32.577 mm^{-1}
Reflections collected	2000 ($R_{(int)} = 0.0408$)
Data, restraints, parameters	224, 0, 18
Goodness of fit on $\|F\|^2$	1.149
Final R indices [$I > 4\sigma(I)$]	$R1$=0.0204, $wR2$=0.0450
R indices (all data)	$R1$=0.0226, $wR2$=0.0455
Largest difference peak and hole	1.917 and −1.477 e Å^{-3}

maintained at 60 mm. The reflections are collected over a range of 3° to 62° in 2θ.

Electrical resistivity is measured on single crystals using the four-probe technique with a Linear Research ac resistance bridge (LR700, $f = 17$ Hz). The Quantum Design (QD) Magnetic Property Measurement System (MPMS) is used for temperature control. Samples are sliced into thin rectangular bars (approximately $0.9 \times 0.45 \times 0.04$ mm), and platinum wires are attached to the samples with Dupont 4929N silver paint. The contact resistances are less than 2 Ω.

Magnetization is measured using a QD-VersaLab vibrating-sample magnetometer (VSM). The standard option is used in the temperature range 50–400 K, and the oven option in the range 300–1000 K. Loctite 435 and Zircar cement are used to attach the samples in the standard and oven options, respectively. Field-dependent magnetization isotherms are also measured down to 2 K in a MPMS. The details of sample mounting and the experimental determination of the demagnetization factor along the easy axis are discussed in Refs. [12,13].

III. COMPOSITION AND STRUCTURAL PROPERTIES

A. Single crystal: Characterization and structure

A picture of as-grown $Ce_{1.66}Mg_{1.34}Co_9$ single crystals, a Laue backscattered photograph, and single-crystal surface diffracted monochromatic XRD data collected via a Rigaku MiniFlex II diffractrometer with Bragg-Brentano geometry [14] are presented in Figs. 2(a), 2(b), and 2(c), respectively. Both Laue and monochromatic single-crystal XRD data confirm that the single crystals grow with a planar morphology with the c axis perpendicular to the plates.

The crystallographic data obtained from the single crystal x-ray diffraction for $Ce_{1.66}Mg_{1.34}Co_9$ grown out of a $Ce_9Mg_{24}Co_{67}$ initial melt are summarized in Tables I and II. Figure 2(d) shows a powder x-ray-diffraction pattern of the crushed single crystals which has some noticeable mismatch in an observed and Rietveld refined intensity of $\{00l\}$ families of the peaks, indicating a degree of preferred orientation in the powder sample. As mentioned above, the relatively small crystal size makes it difficult to acquire enough powder sample to obtain less noisy XRD data and better statistics in the Rietveld refinement. To reduce the intensity mismatch, a preferred orientation correction is employed in the Rietveld refinement using spherical harmonics up to 12th order and absorption correction for platelike grains in the powder sample. The Rietveld refined lattice parameters for powder XRD data of the single crystal $Ce_{1.66}Mg_{1.34}Co_9$ are $a = 4.923(1)$ Å and $c = 24.026(1)$ Å, with $R_p = 0.09$, which is in close agreement (within 2σ to 3σ) with the single-crystal XRD data as shown in Table I. The single crystal XRD composition is $Ce_{13.92}Mg_{11.08}Co_{75}$ ($Ce_{1.662(4)}Mg_{1.338(4)}Co_9$). Although we do not make a quantitative compositional analysis measurement on the single-crystal sample with EDS (the crystals are too thin to readily polish, and small droplets of Mg-rich flux is on their surfaces), we can detect the minor presence of Ta (up to 1 at. %), most likely caused by a slight dissolution of the inner wall surfaces of a Ta reaction container and diffusion of Ta atoms into the reaction liquid during a long-term dwelling process at a maximum temperature of 1200 °C, as well as at ramping down to 1100 °C over 75 h. However, an attempt to solve the crystal structure along with inclusion of Ta in any Wyckoff sites or interstitial sites is unsuccessful. We believe that Ta is distributed in our crystals in the form of nanosized precipitates rather than incorporated into interstices of the crystal structure.

The crystal structure of $Ce_{3-x}Mg_xCo_9$ is rhombohedral and belongs to the $PuNi_3$-type structure [5]. Similar to the

TABLE II. Atomic coordinates and equivalent isotropic displacement parameters (Å$^2 \times 10^{-3}$) for $Ce_{1.66}Mg_{1.34}Co_9$. $U_{(eq)}$ is defined as one third of the trace of the orthogonalized U_{ij} tensor.

Atom	Wyckoff site	Occupancy	x	y	z	$U_{(eq)}$
Ce(1)	3a	1	0	0	0	14(1)
Ce(2)	6c	0.338(4)	0	0	0.1414(1)	12(1)
Mg(2)	6c	0.662(4)	0	0	0.1414(1)	12(1)
Co(1)	3b	1	0	0	$\frac{1}{2}$	11(1)
Co(2)	6c	1	0	0	0.3339(1)	17(1)
Co(3)	18h	1	0.5014(1)	0.4986(1)	0.0840(1)	11(1)

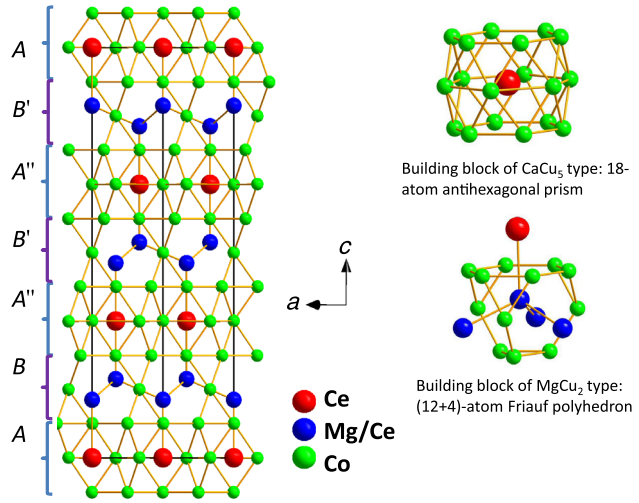

FIG. 3. The crystal structure for $Ce_{3-x}Mg_xCo_9$ showing the stacking sequence of a $CaCu_5$-type plane (A) and a $MgCu_2$-type plane (B) visualized along the [010] direction.

$R_{3-x}Mg_xNi_9$ series, the Co-containing structure is an intergrowth of $CaCu_5$-type (A) and $MgCu_2$-type (B) building blocks with a repeating sequence of $ABA'B'A''B''A$, as shown in Fig. 3. Here, A', B' and A'', B'' are introduced to show the relative translation of the growth layers with respect to the c axis during stacking. There are two independent sites for Ce atoms in this structure: one 3a site is located at the center of a face-shared antihexagonal prism defined by 18 Co atoms, and the other 6c site is surrounded by 12 Co atoms defining a truncated tetrahedron plus four capping atoms at longer distances. As expected from the polyhedra volume, the statistically distributed Ce/Mg mixtures prefer to occupy the Wyckoff 6c site, with its smaller volume.

B. Polycrystalline samples: Composition and lattice parameters

The nominal and EDS compositions of the polycrystalline samples are presented in Table III along with the Rietveld refined percentage of the majority phase in the sample. The SEM images for mixed and predominantly single-phase $Ce_{3-x}Mg_xCo_9$ samples are presented in Fig. 4.

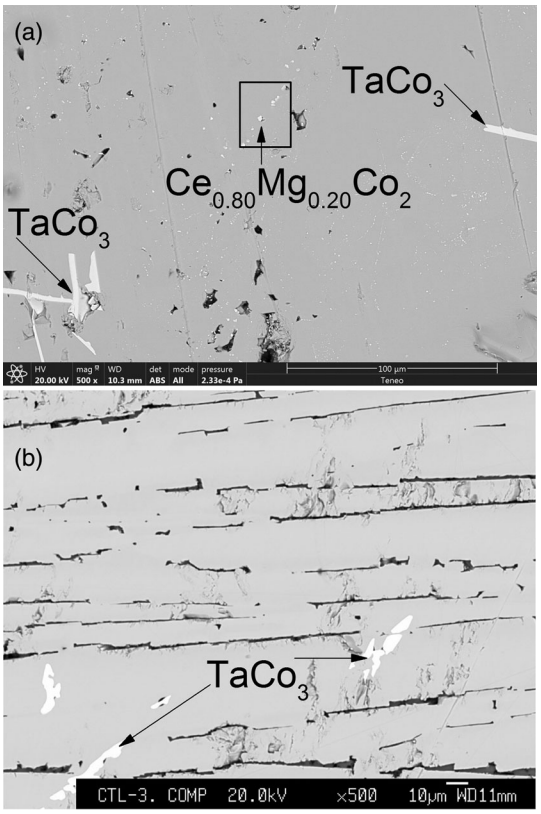

FIG. 4. SEM images of mixed-phase and predominantly single-phase $Ce_{3-x}Mg_xCo_9$ samples. (a) Nominal $Ce_{2.25}Mg_{0.75}Co_9$, which gives a mixture of $Ce_{2.40}Mg_{0.60}Co_9$ (majority phase) and $Ce_{0.80}Mg_{0.20}Co_2$ (minority phase demonstrated as faint small white spots along the diagonal of the black box) and large white stripes of the $TaCo_3$ impurity phase. (b) Predominantly single-phase $Ce_{1.89}Mg_{1.11}Co_9$ along with some traces of $TaCo_3$ impurity. The black parallel grooves in the image represent the cracks in the polished sample.

TABLE III. The comparison of the loaded compositions with the EDS-determined composition. A nominal presence of Ta (up to 1 at. %) is found in the homogeneous $Ce_{3-x}Mg_xCo_9$ samples. Some of the higher-Mg samples show traces of a $TaCo_3$ impurity phase, and low-Mg content samples show a $TaCo_2$ phase.

Loaded composition (nominal)	EDS composition	Rietveld refinement % of majority phase: $Ce_{3-x}Mg_xCo_9$
$CeCo_3$ (arc melted and annealed at 900 °C for 7 d)	$CeCo_3 + CeCo_2$	≥88%
$Ce_{2.75}Mg_{0.25}Co_9$	$Ce_{2.82}Mg_{0.18}Co_9 + Ce_{0.86}Mg_{0.14}Co_2 + TaCo_2$	≥67%
$Ce_{2.50}Mg_{0.5}Co_9$	$Ce_{2.66}Mg_{0.34}Co_9 + Ce_{0.77}Mg_{0.23}Co_2$	≥76%
$Ce_{2.25}Mg_{0.75}Co_9$	$Ce_{2.40}Mg_{0.60}Co_9 + Ce_{0.80}Mg_{0.20}Co_2$	≥80%
$Ce_2Mg_{1.0}Co_9$	$Ce_{2.18}Mg_{0.82}Co_9$	Approximately single phase
$Ce_{1.67}Mg_{1.33}Co_9$	$Ce_{1.89}Mg_{1.11}Co_9$	Approximately single phase
$Ce_{1.5}Mg_{1.5}Co_9$	$Ce_{1.77}Mg_{1.23}Co_9$	Approximately single phase
$Ce_{1.33}Mg_{1.67}Co_9$	$Ce_{1.65}Mg_{1.35}Co_9$	Approximately single phase
$CeMg_2Co_9$	$Ce_{1.42}Mg_{1.58}Co_9 + MgCo_2 + Co$	≥50%

Figure 4(a) shows the mixed-phase sample that forms out of a nominal composition $Ce_{2.25}Mg_{0.75}Co_9$, and Fig. 4(b) shows the predominantly single-phase sample with EDS composition $Ce_{1.89}Mg_{1.11}Co_9$. In addition, Table III summarizes a phase analysis based on powder XRD data.

The crystallographic information file obtained from single-crystal XRD is used to perform Rietveld refinement of the powder XRD data of polycrystal samples listed in Table III. Rietveld refined XRD patterns for multiple-phase polycrystalline samples (nominal $Ce_{2.75}Mg_{0.25}Co_9$ with $R_p = 0.09$, and $Ce_{2.50}Mg_{0.50}Co_9$ with $R_p = 0.10$), and single-phase polycrystalline $Ce_{1.89}Mg_{1.11}Co_9$ (EDS composition) with $R_p = 0.08$ are presented in Figs. 5, 6, and 7, respectively. The melt-annealed nominal $Ce_{2.75}Mg_{0.25}Co_9$ sample contains approximately 67% $Ce_{2.82}Mg_{0.18}Co_9$ phase, about 23% of $Ce_{0.86}Mg_{0.14}Co_2$, and roughly 10% of $TaCo_2$ inferred from Rietveld refinement. The $TaCo_2$ phase is not observed in the nominal $Ce_{2.50}Mg_{0.5}Co_9$ and higher content of Mg, as shown in Figs. 6 and 7. An unidentified XRD peak is observed in the nominal $Ce_{2.50}Mg_{0.50}Co_9$ sample shown in Fig. 6; however, the $TaCo_2$ phase is almost reduced to zero in comparison to the nominal composition $Ce_{2.75}Mg_{0.25}Co_9$ shown in Fig. 5. However, traces of the $TaCo_3$ phase are observed in predominantly single-phase $Ce_{3-x}Mg_xCo_9$ samples. These results, combined with the fact that even pure (Mg = 0) $CeCo_3$ remains mixed phase after 7 d of annealing, suggest that Mg assists the annealing of polycrystalline $Ce_{3-x}Mg_xCo_9$ samples.

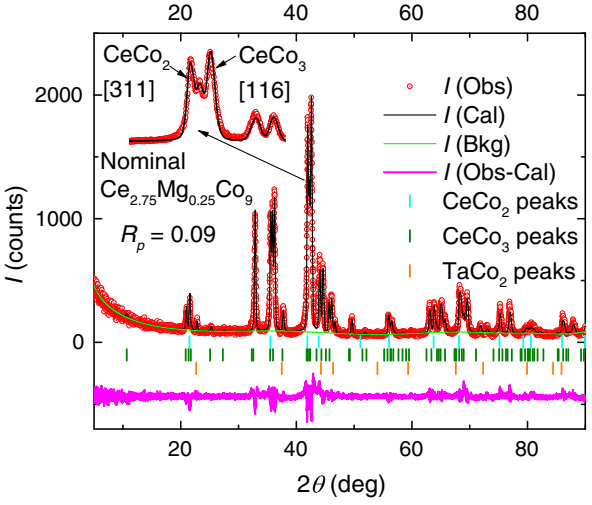

FIG. 5. A typical example of a multiphase polycrystalline XRD pattern for a nominal $Ce_{2.75}Mg_{0.25}Co_9$ sample. The enlarged peak at the left top of the graph shows the broadening of the highest-intensity peak of $Ce_{3-x}Mg_xCo_9$ around a 2θ value of 42° due to the presence of a Mg-doped $CeCo_2$ diffraction peak. *I* (Obs), *I* (Cal), and *I* (Bkg) are the experimental, Rietveld refined, and instrumental background data, respectively. The lower section of the graph shows the Bragg's-peak positions with different-colored vertical lines for phases shown in the graph and the differential x-ray diffractrogram *I* (Obs-Cal).

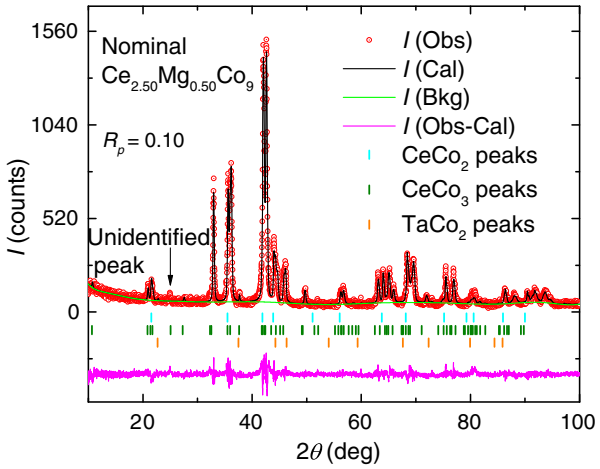

FIG. 6. Powder XRD pattern for a nominal $Ce_{2.50}Mg_{0.50}Co_9$ sample. The $TaCo_2$ phase is almost not detectable for XRD; however, an unidentified XRD peak is observed at around the 2θ value of 25°. *I* (Obs), *I* (Cal), and *I* (Bkg) are the experimental, Rietveld refined, and instrumental background data, respectively. The lower section of the graph shows the Bragg's-peak positions with different-colored vertical lines for phases shown in the graph and the differential x-ray diffractrogram *I* (Obs-Cal).

For nominal values of $x = 2$ and higher, $Ce_{3-x}Mg_xCo_9$ can no longer be considered a clear majority phase with the presence of a significant amount of $CoMg_2$ and Co. Looking at the composition of the $Ce_{3-x}Mg_xCo_9$ alloys from EDS, it seems that $x \approx 1.4$ is the maximum solid solubility. In the $Nd_{3-x}Mg_xCo_9$ alloys, the structure changes from the trigonal structure for $x \leq 1.5$ to a tetragonal structure at $x = 2$ (YIn_2Ni_9 type) [6]. The solubility range of Mg in $CeCo_3$ is therefore similar,

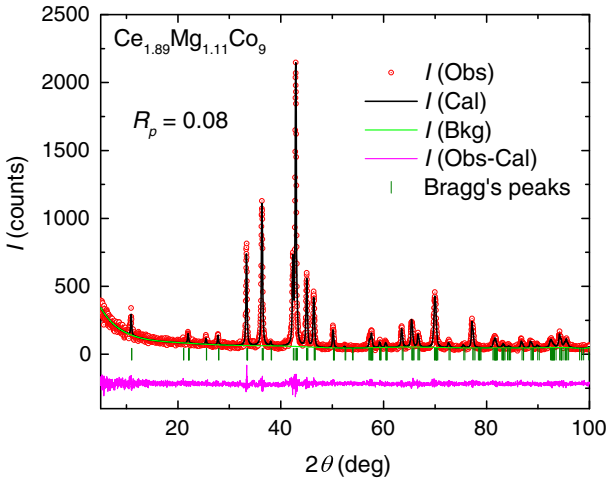

FIG. 7. A typical example of a predominantly single-phase polycrystalline XRD pattern for an EDS-characterized $Ce_{1.89}Mg_{1.11}Co_9$ sample. *I* (Obs), *I* (Cal), and *I* (Bkg) are the experimental, Rietveld refined, and instrumental background data, respectively. The lower section of the graph shows the Bragg's-peak positions with olive vertical lines and the differential x-ray diffractrogram *I* (Obs-Cal).

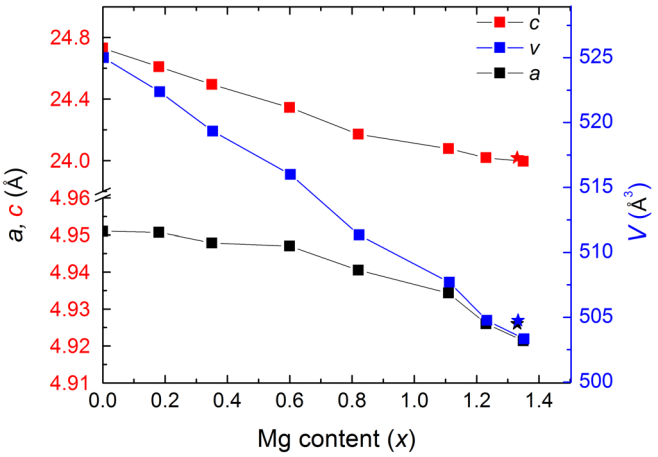

FIG. 8. Variation of the lattice parameters (a,c) and the unit-cell volume (v) of polycrystalline $Ce_{3-x}Mg_xCo_9$ with Mg content inferred from EDS. Cubic $Ce_{1-x}Mg_xCo_2$-type impurity phases are obtained for $x \leq 0.6$, and predominantly single-phase $Ce_{3-x}Mg_xCo_9$ is obtained for $0.6 < x \leq 1.4$. The lattice parameters for single-crystal $Ce_{1.66}Mg_{1.34}Co_9$ are presented with corresponding color stars. The uncertainty in the refined lattice parameters is less than 0.01% of the reported lattice parameters and is too small to clearly show as an error bar in the diagram.

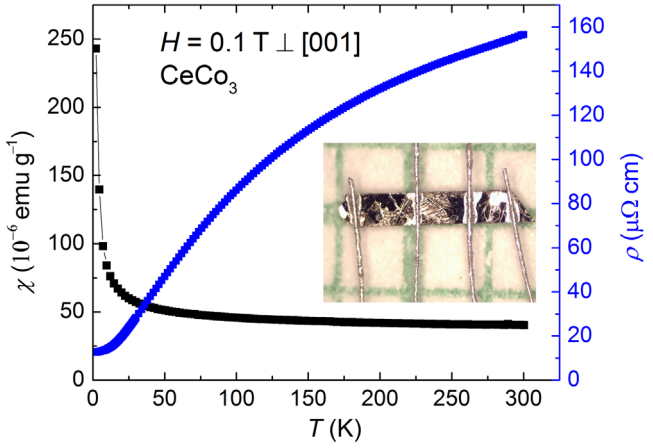

FIG. 9. Temperature-dependent susceptibility ($H = 0.1\text{T} \perp [001]$) and electrical resistivity (excitation current $\perp$ to [001]) of a $CeCo_3$ single crystal. (Inset) Resistivity bar for the four-probe measurement. The sample is 60 μm thick.

but we do not observe a phase corresponding with the YIn_2Ni_9-type structure for $x \geq 2$. Instead, a three-phase region of $MgCo_2$, $Ce_{3-x}Mg_xCo_9$, and Co is observed (see Table III). The compositional range of our $Ce_{3-x}Mg_xCo_9$ samples is summarized in Fig. 1.

The variation of the polycrystalline lattice parameters and unit-cell volume as a function of the Mg content in the $Ce_{3-x}Mg_xCo_9$ phase, as determined using EDS, is shown in Fig. 8. As expected, the substitution of Mg for Ce results in a reduction of the unit-cell volume, similar to the case with $Nd_{3-x}Mg_xCo_9$ alloys [6]. Neither the a nor the c lattice parameter follows a linear relation with Mg content x. The variation in the a lattice parameter shows a slight positive deviation, and the c lattice parameter shows a slight negative deviation starting in the middle of the single-phase region. The negative deviation of lattice parameter c might indicate that the covalent bonding is increased along that direction. It should be noted that the lattice parameters (a, c, v) and composition inferred from the single-crystal x-rays (shown as the corresponding color ⋆s) agree very well with what we infer from EDS measurements on the polycrystalline samples.

IV. MAGNETIC PROPERTIES

Previously reported data do not agree on the magnetic properties of the parent compound, $CeCo_3$. Lemaire reported on $CeCo_3$ as a ferromagnetic material with Curie temperature 78 K [15]. Buschow identified it as a Pauli-paramagnetic phase; however, he left room for further investigation by mentioning that $CeCo_3$ could be ferromagnetic below 10 K [16]. To clarify this issue, we measure the temperature-dependent magnetization and electric resistivity of our single-crystal samples down to 2 K, as shown in Fig. 9. The magnetization data show no signature of a phase transition, and they are only weakly temperature dependent and are consistent with a Pauli paramagnet and an impurity tail below 20 K. Assuming the Curie tail is because of the Ce^{3+} magnetic ions in the single-crystal $CeCo_3$ sample, magnetic susceptibility is fitted to the Curie-Weiss law up to 150 K as

$$\chi(T) = \chi_0 + \frac{C}{T-\theta},$$

where χ_0 is the high-temperature asymptotic susceptibility, C is the Curie constant, and θ is the Curie-Weiss temperature. The concentration of Ce^{3+} ions is estimated to be approximately 20% (with $\theta = 3.8$ K) using the spin-only moment of $2.54\mu_B$ per Ce^{3+} ion. The electrical resistivity does not show any signature of a loss of spin-disorder scattering, which would be anticipated for a magnetic phase transition.

The temperature dependences of the magnetization data of the single-phase $Ce_{3-x}Mg_xCo_9$ polycrystalline samples are shown in Fig. 10. A rapid increase of the magnetization upon cooling below the Curie temperature is observed for $x = 0.82$–1.35, indicating the appearance of ferromagnetism upon Mg substitution.

The Curie temperature T_C is estimated as the cross-point of linear extrapolations of two tangents to the magnetization curve around the point of inflection, as indicated on the curves $x = 1.11$ and $x = 1.23$ in Fig. 10. The variation of T_C with Mg substitution is shown in the inset. The Curie temperature increases with Mg concentration and reaches as high as 450 K for $x = 1.35$.

The substitution of Mg for Ce changes a Pauli paramagnet ($CeCo_3$) into a ferromagnet that has T_C increase

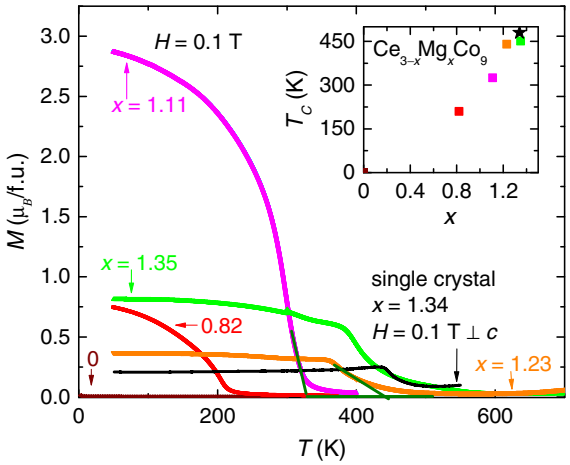

FIG. 10. Temperature-dependent magnetization of single-crystal ($x = 0$ and 1.34), polycrystalline $Ce_{3-x}Mg_xCo_9$ measured under a magnetic field of 0.1 T. The arrow-pointed Mg content (x) for each $M(T)$ graph is inferred from EDS analysis. The olive-colored straight lines above and below the point of inflection of $M(T)$ data for $x = 1.11$ and $x = 1.23$ shows the scheme for inferring the Curie temperature. (Inset) The obtained Curie temperatures and the Mg-content phase diagram. ⋆ indicates the Curie temperature inferred from the tangent intersection scheme for a single-crystal $Ce_{1.66}Mg_{1.34}Co_9$ sample on the $M(T)$ data measured along the hard axis of the plate.

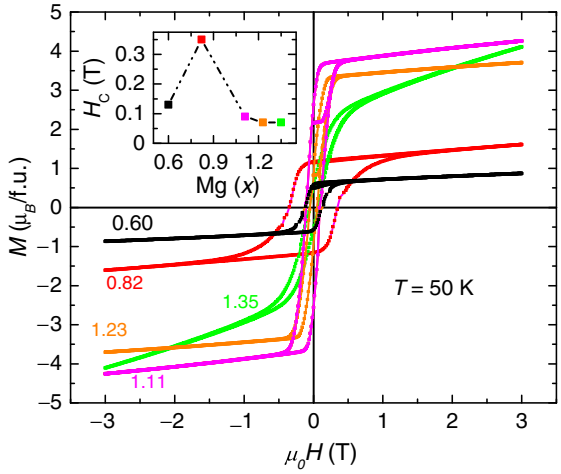

FIG. 11. Magnetic hysteresis loop of various annealed polycrystalline $Ce_{3-x}Mg_xCo_9$ samples at 50 K. The values of the Mg content are from an EDS analysis. (Inset) Variation of the observed coercivity fields of the samples as a function of the Mg content.

with Mg content. The most likely reason for this increment is associated with valency and band filling. In $CeCo_3$, the Ce is essentially nonmoment bearing, which implies a Ce^{4+} valency. As Mg^{2+} is added, there is a clear change in band filling that most likely leads to Stoner-type magnetism associated with the Co $3d$ bands. Further work, both computational and experimental, will be needed to better appreciate the origin of the observed ferromagnetism.

Figure 11 shows the magnetic hysteresis curves of various polycrystals along with the observed coercivity fields at 50 K (see the inset). The coercivity field increases with Mg content, becomes maximal (about 0.35 T) for $x = 0.82$, then decreases. The observation of coercivity is consistent with the axial nature of the magnetic anisotropy, as detailed below. The abruptly increased coercivity for $x = 0.82$ and the spontaneous magnetization for $x = 1.11$ magnesium-containing phases are reproduced in multiple samples. It should be noted that differing saturation values for differing x values are most likely due to the nonrandom distribution of grains in these as-cast samples. In addition, the nonsaturating behavior of the $x = 1.35$ sample indicates either the presence of the preferred orientations of the grains with their hard axis along the applied field or the presence of some anisotropic magnetic impurity in the sample. The former argument can be easily visualized in the $M(T)$ data, as the $x = 1.35$ polycrystalline sample and the single-crystal $Ce_{1.66}Mg_{1.34}Co_9$ $M(T)$ data along the hard axis are almost identical in nature, as shown in Fig. 10. The fact that the as-cast samples show coercivity is promising for the development of permanent magnets out of this system.

Our single-crystal sample can provide further insight into this system's promise as a permanent-magnet material. Figure 12 shows the temperature dependence of the magnetization parallel and perpendicular to the c axis of the single crystal of $Ce_{1.66}Mg_{1.34}Co_9$ up to 550 K. The c axis is the easy axis of magnetization, and the saturation magnetization at low temperature is 8 μ_B/f.u.. The spontaneous-magnetization data points for $Ce_{1.66}Mg_{1.34}Co_9$,

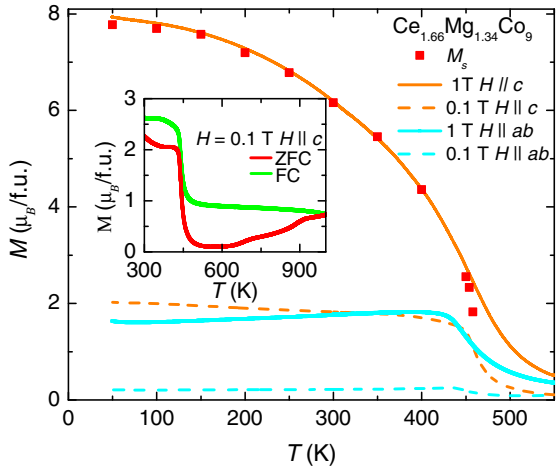

FIG. 12. Anisotropic temperature-dependent magnetization for $Ce_{1.66}Mg_{1.34}Co_9$ at various applied fields and directions. The dashed lines represent $H = 0.1$ T, and the solid lines show $H = 1.0$ T. Individual data points (the red squares) indicate spontaneous magnetization. M_S is inferred from $M(H)$ isotherms. (Inset) Zero-field-cooled (ZFC) and field-cooled (FC) magnetization data along the easy axis of magnetization to temperature above the sample decomposition point.

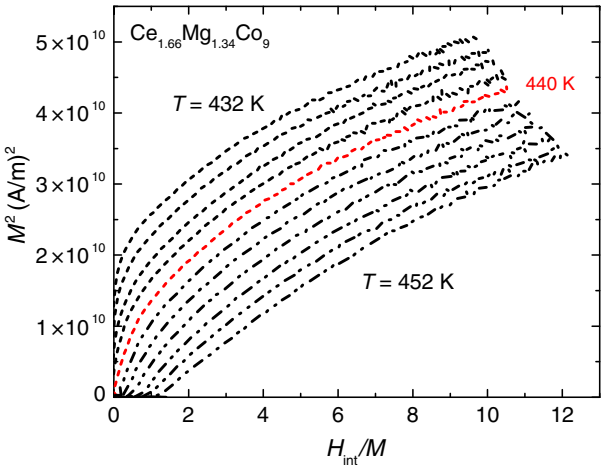

FIG. 13. Arrott plot for a $Ce_{1.66}Mg_{1.34}Co_9$ single crystal within a temperature range of 432 to 452 K at steps of 2 K between adjacent curves. The Curie temperature is determined to be 440 K.

represented as red squares, are obtained by the Y intercept of the linear fitting of the high field $M(H)M(H)$ data (>1.5 T) in the first quadrant. No hysteresis is observed in the $M(H)$ loops. The absence of hysteresis in the $M(H)$ isotherms measured in the single crystals is due to an absence of grain boundaries, defects, and impurity atoms capable of pinning the ferromagnetic domains. When measurements are performed up to 1000 K, we notice a nonreproducibility of the results, as shown in the inset of Fig. 12. Thermogravimetric analysis (not shown here) shows evidence for a decomposition of the samples. This degradation is not observed when limiting the measurements to a maximum temperature of 550 K.

An Arrott plot with several isotherms near the Curie temperature is shown in Fig. 13. The internal magnetic field H_{int} is determined using the relation $H_{\text{int}} = H_{\text{app}} - N * M$,

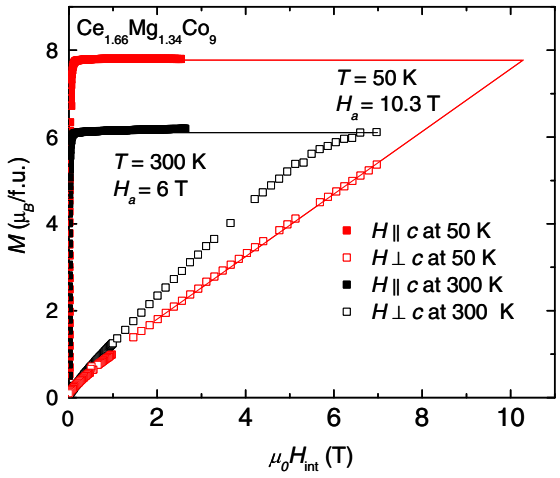

FIG. 14. Anisotropic field-dependent magnetization of $Ce_{1.66}Mg_{1.34}Co_9$ at 50 K ($H_a \approx 10$ T) and 300 K ($H_a \approx 6$ T).

where H_{app} is the applied field, N is the demagnetization factor which is experimentally determined along the easy axis ($N_c = 0.78$) [12,13], and M is the magnetization. The Arrott curves are not linear, indicating that $Ce_{1.66}Mg_{1.34}Co_9$ does not follow the mean-field theory. The Curie temperature of $Ce_{1.66}Mg_{1.34}Co_9$ is 440 K since the Arrott curve corresponding to 440 K passes through the origin. This temperature is comparable to the values of T_C obtained from polycrystals of similar composition (see the inset of Fig. 10).

The magnetocrystalline anisotropy field is determined to be about 10 T ($T = 2$ K) and approximately 6 T ($T = 300$ K) for a $Ce_{1.66}Mg_{1.34}Co_9$ single-crystal sample, as shown in Fig. 14. The anisotropy field is determined by a linear extrapolation of the observed moment along the plane up to the saturation moment.

The anisotropy energy is quantified by using a Sucksmith-Thompson plot for field-dependent magnetization data along the plane, as shown in Fig. 15. In the Sucksmith-Thompson plot, the ratio of the magnetizing field with hard-axis magnetization data is related to the anisotropy constants K_1 and K_2, the saturation magnetization M_s, and the hard-axis magnetization ($M_\perp$) as shown in the following equation [17,18]:

$$\frac{\mu_0 H}{M_\perp} = \frac{2K_1}{M_s^2} + \frac{4K_2}{M_s^4} M_\perp^2 . \tag{1}$$

The intercept of the Sucksmith-Thompson plot gives the anisotropy constant K_1, and the slope gives the anisotropy

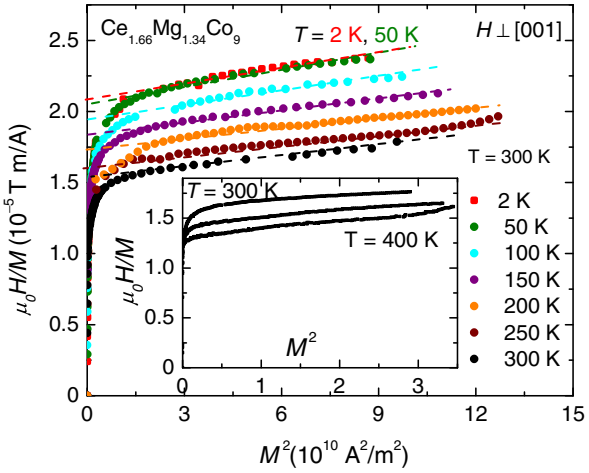

FIG. 15. Sucksmith-Thompson plot for $Ce_{1.66}Mg_{1.34}Co_9$ to obtain anisotropy constants K_1 and K_2. The field-dependent magnetization data are measured up to 7 T along the hard axis of magnetization. The dotted straight lines are the linear fits to $[(\mu_0 H)/M]$ at high-field magnetization data to obtain the intercepts and slopes of the isotherms. (Inset) Sucksmith-Thompson plots for VSM data measured along the hard axis ($H \perp [001]$) up to the 3-T field. K_1 and K_2, obtained using the VSM data, are matched to the MPMS data at 300 K.

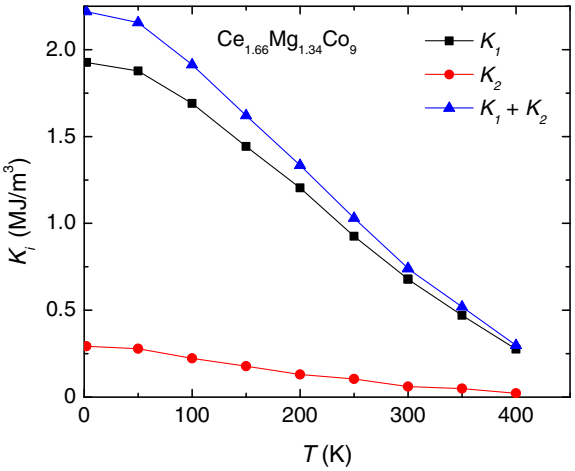

FIG. 16. Temperature dependent anisotropy energy constants for $Ce_{1.66}Mg_{1.34}Co_9$. The anisotropy constants are determined from the Sucksmith-Thompson plot. K_1 and K_2 values up to 300 K are measured using MPMS, and higher-temperature data are measured using VSM.

constant K_2. Figure 16 shows the temperature variation of the measured anisotropy constants. There is a slight mismatch (<2%) in the anisotropy data above and below the 300-K value obtained from the VSM and MPMS data. The VSM data are scaled to the MPMS data at 300 K since the slope of the Sucksmith-Thompson plot is better determined with a higher applied field. Here, the total anisotropy energy of $Ce_{1.66}Mg_{1.34}Co_9$ is determined to be 2.2 MJ/m^3. Such high anisotropy energy density makes $Ce_{1.66}Mg_{1.34}Co_9$ a potential candidate for permanent-magnet applications.

V. CONCLUSIONS

In this paper, we investigate the effect of Mg substitution into the Ce_3Co_9 (e.g., $CeCo_3$) binary phase where Mg partially replaces the Ce atom on the 6*c* crystallographic site, giving rise to the $Ce_{3-x}Mg_xCo_9$ solid solution for $0 \leq x \lesssim 1.4$. The substituted Mg induces ferromagnetism; the Curie temperature of the solid solution increases with a higher content of Mg and becomes maximal (450 K) at Mg content $x = 1.35$. The magnetic anisotropy is determined for a self-flux-grown $Ce_{1.66}Mg_{1.34}Co_9$ single crystal. The uniaxial-anisotropy field is determined to be approximately 10 T at 2 K and about 6 T at 300 K. The anisotropy energy density is determined to be 2.2 MJ/m^3 at 2 K. With these observed magnetic properties, the $Ce_{3-x}Mg_xCo_9$ solution shows the potential to be used as a permanent magnet.

ACKNOWLEDGMENTS

We would like to thank Dr. T. Kong for the useful discussions. Dr. Warren Straszheim is acknowledged for doing SEM on various samples. This research was supported by the Critical Materials Institute, an Energy Innovation Hub funded by the U.S. Department of Energy, Office of Energy Efficiency and Renewable Energy, Advanced Manufacturing Office. Q. L. is supported by the office of Basic Energy Sciences, Materials Sciences Division, U.S. DOE. This work was performed at the Ames Laboratory, operated for the DOE by Iowa State University under Contract No. DE-AC02-07CH11358.

[1] G. B. Haxel, J. B. Hedrick, and G. J. Orris, U.S. Geological Survey Fact Sheet No. 087-02, 2002.
[2] Pradyot Patnaik, *Handbook of Inorganic Chemicals* (McGraw-Hill, New York, 2003).
[3] Feng Xie, Ting An Zhang, David Dreisinger, and Fiona Doyle, A critical review on solvent extraction of rare earths from aqueous solutions, Miner. Eng. **56**, 10 (2014).
[4] Arjun K. Pathak, Mahmud Khan, Karl A. Gschneidner, Ralph W. McCallum, Lin Zhou, Kewei Sun, Kevin W. Dennis, Chen Zhou, Frederick E. Pinkerton, Matthew J. Kramer, and Vitalij K. Pecharsky, Cerium: An unlikely replacement of dysprosium in high performance NdFeB permanent magnets, Adv. Mater. **27**, 2663 (2015).
[5] R. V. Denys, A. B. Riabov, R. Černý, I. V. Koval'chuk, and I. Yu. Zavaliy, New $CeMgCo_4$ and Ce_2MgCo_9 compounds: Hydrogenation properties and crystal structure of hydrides, J. Solid State Chem. **187**, 1 (2012).
[6] V. V. Shtender, R. V. Denys, V. Paul-Boncour, I. Yu. Zavaliy, Yu. V. Verbovytskyy, and D. D. Taylor, Crystal structure, hydrogen absorption-desorption behavior and magnetic properties of the $Nd_{3-x}Mg_xCo_9$ alloys, J. Alloys Compd. **695**, 1426 (2017).
[7] M. I. Bartashevich, K. Koui, T. Goto, M. Yamaguchi, I. Yamamoto, and F. Sugaya, Magnetic properties of $NdCo_3$ and its γ-phase hydride $NdCo_3H_{4.1}$, J. Alloys Compd. **202**, 7 (1993).
[8] Paul C. Canfield and Ian R. Fisher, High-temperature solution growth of intermetallic single crystals and quasicrystals, J. Cryst. Growth **225**, 155 (2001).
[9] H. Okamoto, Ce-Co phase diagram, in *ASM Alloy Phase Diagrams Database*, edited by P. Villars, H. Okamoto, and K. Cenzual (ASM International, Materials Park, OH, 1990).
[10] A. C. Larson and R. B. Von Dreele, Los Alamos National Laboratory Report No. LAUR 86-748, 2004.
[11] Brian H. Toby, EXPGUI, a graphical user interface for GSAS, J. Appl. Crystallogr. **34**, 210 (2001).
[12] Tej N. Lamichhane, Valentin Taufour, Srinivasa Thimmaiah, David S. Parker, Sergey L. Bud'ko, and Paul C. Canfield, A study of the physical properties of single crystalline Fe_5B_2P, J. Magn. Magn. Mater. **401**, 525 (2016).
[13] Tej N. Lamichhane, Valentin Taufour, Morgan W. Masters, David S. Parker, Udhara S. Kaluarachchi, Srinivasa Thimmaiah, Sergey L. Bud'ko, and Paul C. Canfield, Discovery of ferromagnetism with large magnetic anisotropy in ZrMnP and HfMnP, Appl. Phys. Lett. **109**, 092402 (2016).
[14] A. Jesche, M. Fix, A. Kreyssig, W. R. Meier, and P. C. Canfield, X-ray diffraction on large single crystals

using a powder diffractometer, Philos. Mag. **96**, 2115 (2016).

[15] R. Lemaire, Magnetic properties of the intermetallic compounds of cobalt with the rare earth metals and yttrium, Cobalt **33**, 201 (1966).

[16] K. H. J. Buschow, Magnetic properties of $CeCo_3$, Ce_2Co_7 and $CeNi_3$ and their ternary hydrides, J. Less-Common Met. **72**, 257 (1980).

[17] W. Sucksmith and J. E. Thompson, The magnetic anisotropy of cobalt, Proc. R. Soc. A **225**, 362 (1954).

[18] Valentin Taufour, Srinivasa Thimmaiah, Stephen March, Scott Saunders, Kewei Sun, Tej Nath Lamichhane, Matthew J. Kramer, Sergey L. Bud'ko, and Paul C. Canfield, Structural and Ferromagnetic Properties of an Orthorhombic Phase of MnBi Stabilized with Rh Additions, Phys. Rev. Applied **4**, 014021 (2015).